

RSC Advances



This is an *Accepted Manuscript*, which has been through the Royal Society of Chemistry peer review process and has been accepted for publication.

Accepted Manuscripts are published online shortly after acceptance, before technical editing, formatting and proof reading. Using this free service, authors can make their results available to the community, in citable form, before we publish the edited article. This *Accepted Manuscript* will be replaced by the edited, formatted and paginated article as soon as this is available.

You can find more information about *Accepted Manuscripts* in the [Information for Authors](#).

Please note that technical editing may introduce minor changes to the text and/or graphics, which may alter content. The journal's standard [Terms & Conditions](#) and the [Ethical guidelines](#) still apply. In no event shall the Royal Society of Chemistry be held responsible for any errors or omissions in this *Accepted Manuscript* or any consequences arising from the use of any information it contains.

The ground-state structure and physical properties of ReB₃ and IrB₃ predicted from first principles

Qian Yan¹, Yuan Xu Wang^{1,2, a}, Bing Wang¹, Jueming Yang¹ and Gui Yang¹

¹*Institute for Computational Materials Science,
School of Physics and Electronics, Henan University,
Kaifeng 475004, People's Republic of China and*

²*Guizhou Provincial Key Laboratory of Computational Nano-Material science,
Institute of Applied Physics, Guizhou Normal College,
Guiyang 550018, People's Republic of China*

Abstract

ReB₃ has been synthesized and was reported to have the symmetry of $P6_3/mmc$. [Acta Chem. Scand. 1960, 14, 733] However, we find that this structure is not stable due to its positive formation energy. In 2009, IrB_{1.35} and IrB_{1.1} has been synthesized and were considered to be superhard.[Chem. Mater. 2007, 21, 1407; ACS Appl. Mater. Interfaces 2010, 2, 581] Inspired by these, we explored the possible crystal structures of ReB₃ and IrB₃ by using the developed particle swarm optimization algorithm. We predicted that $P\bar{6}m2$ -ReB₃ and $Amm2$ -IrB₃ are the ground-state phases of ReB₃ and IrB₃, respectively. The stability, elastic properties, and electronic structures of the predicted structures were studied by first-principles calculations. The negative calculated formation enthalpies for $P\bar{6}m2$ -ReB₃ and $P6_3/mmc$ -ReB₃ indicate that they are stable and can be synthesized under ambient pressure. Their dynamical stability is confirmed by calculated phonon dispersion curves. The predicted $P6_3/mmc$ -ReB₃ has the highest hardness among these predicted structures. The calculated density of state shows that these predicted structures are metallic. The chemical bonding feature of the predicted ReB₃ and IrB₃ was investigated by analyzing their electronic localization function.

Keywords: Particle swarm optimization, formation enthalpy, dynamical stability, elastic properties

^a E-mail: wangyx@henu.edu.cn

I. INTRODUCTION

The term hardness was created by the French scientist R.A.F de Réaumur in 1722, and it has been a fundamental mechanical property of materials after that.[1] Nowadays, ultracompressible hard materials are extremely useful in industry due to their excellent performance, such as cutting tools, drilling tools, hard coating, and abrasives. Great efforts have been devoted to search new superhard materials. One approach is to synthesizing light element compounds which contain boron, carbon, nitrogen, or oxygen, for instance, diamond, cubic boron nitride (c-BN), and carbon nitrides, etc.[2–4] It is well known that diamond is the hardest material with a measured hardness of 60-120 GPa.[2] However, at high temperature, diamond is not only unstable in presence of oxygen, but also reacts easily with iron-containing materials. These light element compounds are usually synthesized under high temperature and high pressure conditions, which leads to high production costs. Another approach for searching new superhard materials is performed by inserting light elements into the lattice of transition metal, for example ReB_2 . [5–7] The introducing of light elements improves the hardness of transition metal by forming strong covalent interaction between TM and light elements, and between light elements. These compounds usually possess high electron density and strong covalent bonds. Especially, the transition metal borides can be synthesized under ambient pressure, which reduces the cost of synthesis. The synthesis of ReB_2 and its high hardness has lighted the passion for exploring new transition-metal compounds with high hardness.[5–7] Some novel transition-metal borides have been successfully synthesized under ambient pressure, such as OsB_2 , TaB_2 , CrB_4 , and WB_4 . [8–11] They all have high bulk modulus that is not far from the diamond. Therefore, transition metal borides could be promising superhard materials.

5d transition metal triborides have also attracted great attentions. For example, the structure of WB_3 with high hardness has been explored and is debated by many works.[12–15] In 1960, Aronsson et al. reported that they synthesized ReB_3 . [16] However, this structure was suggested to be unstable.[17, 18] Up to now, the structure of ReB_3 is still an open question. In 2009, $\text{IrB}_{1.35}$ has been synthesized with iridium powder and boron powder taken in molar ratio of 1:1.5. Its Vickers hardness decreases from 49.8 to 18.2 GPa as the load increased from 0.49 to 9.81.[19] After that, $\text{IrB}_{1.1}$ was deposited on SiO_2 substrates, and the film was considered to be superhard due to its high Vickers hardness of 43 GPa.[20]

For iridium borides with integral elements ratio, IrB and IrB₂ were investigated by Zhao et al. and Wang et al.[21, 22]. *Pnma*-IrB and the orthorhombic OsB₂-type structure of IrB₂ were considered to be the most energetically stable.

The hardness of TM borides can be improved by increasing the concentration of boron in them. Therefore, in this work, we explore the possible structures of ReB₃ and IrB₃ through the method of the particle-swarm optimization (PSO).[23, 24] The bonding feature, the electronic structure, the mechanical properties of the predicted structures of ReB₃ and IrB₃ were investigated by the first-principles calculations.

II. COMPUTATIONAL DETAIL

In this work, we used CALYPSO to search the potential crystal structures of ReB₃ and IrB₃ with 1-4 formula units(f.u.) in each simulation cell at 0 GPa.[23, 24] The advantage of this approach is that it needs only the chemical compositions of the given compounds at specified external conditions and does not need any structural information. The underlying structure relaxations and properties calculations were performed with the projector-augmented-wave method (PAW) based on the density functional theory (DFT) as implemented in the Vienna ab initio simulation package (VASP).[25, 26] The Perdew-Burke-Ernzerhof generalized gradient approximation (PBE-GGA) was used to treat the exchange-correlation function. Geometry optimization of the structures was achieved through the conjugate gradient algorithm method with a plane wave cutoff energy of 400 eV, and the forces on each ions were well-converged to be less than 5 meV/atom. Both the lattice constants and the atomic positions of the predicted structures were relaxed. For the *k*-point samplings in the Brillouin zone for the hexagonal structures, Γ centered grids were used, and for other structures, the Monkhorst-Pack scheme were used. Formation enthalpy was calculated from the equation $\Delta H = H(\text{MB}_3) - 3H(\text{solid B}) - H(\text{M})$. The solid boron is the α -B₁₂ at 0 GPa. The elastic constants were obtained by the strain-stress method. With the obtained elastic constants C_{ij} , the polycrystalline bulk modulus B and shear modulus G were estimated using the Voigt-Reuss-Hill approximation.[27] Young's modulus Y and Poisson's ratio ν were obtained by using the equations $Y = (9GB)/(3B+G)$ and $\nu = (3B-2G)/(6B+2G)$, respectively. The Debye temperature was calculated from the bulk modulus, shear modulus and so on.

To check the reliability of the method used in this work, we explored the structures of WB_3 and OsB_3 . The previous reported ground-state structure of OsB_3 with $P\bar{6}m2$ symmetry has been successfully predicted by us through the PSO method.[28] Two new structures with the symmetry of $P\bar{3}m1$ and $P6/mmm$ were predicted at the same time. The positive formation energies indicate that they are metastable at 0 GPa. Moreover, the negative and lowest formation energy of $P\bar{6}m2$ - OsB_3 show that it is the ground-state phase of OsB_3 . For WB_3 , at 0 GPa, the earliest discovered $P6_3/mmc$ - WB_3 has been predicted again by us, substantiating the reliability of our method.[13, 29, 30] Moreover, we found some other previous reported structures of WB_3 with the symmetry of $R\bar{3}m$, $P\bar{6}m2$, and $P\bar{3}m1$ by this way.[12, 15] Among these structures, the $R\bar{3}m$ phase possesses the lowest formation energy, which indicates that the $R\bar{3}m$ phase is the ground-state structure of WB_3 .

III. RESULTS AND DISCUSSIONS

A. Structure Property and Stability

We searched the potential crystal structures of ReB_3 and IrB_3 using the PSO methodology. The relaxed lattice parameters, density, and atom volume were tabulated in Table I, and the structures were shown in Fig. 1 and Fig. 2, respectively.

ReB_3 was first synthesized by Aronsson et al. and was suggested to be hexagonal with the symmetry of $P6_3/mmc$. [16] However, several theoretical studies on the experimental ReB_3 suggested that the experimental ReB_3 easily decomposes during the course of synthesis. [17, 18] Gao et al. supposed that the antibonding feature of all Re-B bonds leads to the instability of ReB_3 . By using the PSO method, we found a new structure of $P6_3/mmc$ - ReB_3 , which is lower in energy than the experimental one. At zero pressure, the negative formation energy of the predicted $P6_3/mmc$ - ReB_3 indicates that it is a stable structure. The experimental structure composes of the puckered hexagonal planar boron layer. The shortest Re-B and B-B bond in it are 2.34 and 1.86 Å, respectively. The predicted $P6_3/mmc$ - ReB_3 composes of the puckered hexagon-mesh layers with half of the boron atoms in hexagon-mesh layers being replaced by a pair of vertical boron dimers, and the nearest boron layers tend to offset each other. This boron dimers in the predicted $P6_3/mmc$ - ReB_3 may increase the strength along c -axis compared with the experimental one. We also calculated the bond lengths of the predicted $P6_3/mmc$ - ReB_3 . In this structure, each rhenium atom is coordinated by four

boron atoms, with bond lengths of 2.26-2.32 Å. The boron atoms in it can be divided into two types. The first type is coordinated by one boron atom and one rhenium atom, with bond lengths of 1.85(B-B) and 2.26(Re-B) Å, respectively. The second type is coordinated by two boron atoms and two rhenium atoms, with bond lengths of 1.85(B-B) and 2.32(Re-B) Å, respectively. The shortest Re-B and B-B bond lengths are 2.26 and 1.85 Å, respectively. They are all shorter than those in experimental one. Such shorter Re-B and B-B bonds in the predicted $P6_3/mmc$ -ReB₃ mean the stronger covalent interaction between the adjacent atoms, which is helpful to increasing its stability.

To further explore the origin of the lower energy of the predicted $P6_3/mmc$ -ReB₃ than the experimental structure, we calculated their density of states(DOS) and electronic localization function(ELF), and display them in Fig. 3 and Fig. 4, respectively. As seen in Fig. 3, there is a DOS peak at the Fermi level of the experimental structure, indicating that the experimental structure is not so stable. However, a pseudogap appears near the Fermi level of the DOS of the predicted $P6_3/mmc$ -ReB₃, indicating the high stability of the predicted $P6_3/mmc$ -ReB₃. Moreover, the broad DOS peak from -8 eV to 0 eV indicates the strong hybridization between Re-d and B-p states in the predicted $P6_3/mmc$ -ReB₃, which will increase its stability. The pseudogap of the experimental ReB₃ appears -3.3 eV, which indicates that the excrescent electrons exist in the experimental structure. ELF can directly show the bonding feature of materials. As seen in Fig. 4 (a) and (c), the largest value of ELF between the adjacent B atoms in experimental ReB₃ is much smaller than that of the predicted $P6_3/mmc$ -ReB₃. Thus, the covalency of the B-B bond in the predicted $P6_3/mmc$ -ReB₃ is stronger than that in the experimental structure, which is also helpful for increasing the stability of the predicted $P6_3/mmc$ -ReB₃. Therefore, the stronger covalency of the Re-B and B-B bonding in the predicted $P6_3/mmc$ -ReB₃ will lead to the higher stability of the predicted $P6_3/mmc$ -ReB₃ than the experimentally synthesized ReB₃.

Some new structures have been found at the same time, and the symmetries are $P\bar{6}m2$ and $P\bar{3}m1$, respectively. $P\bar{6}m2$ -ReB₃ has a puckered graphitelike B layer with half of the boron atoms being replaced by a pair of vertical B₂ dimers. The rhenium atom is coordinated by three boron atoms, with bond lengths of 2.24-2.30 Å. There are two types of boron atoms in this compound. One is coordinated by one rhenium atom and two boron atoms, with bond lengths of 2.24(Re-B), 1.66(B-B), and 1.88(B-B) Å, respectively. The other is coordinated by one rhenium atom and two boron atoms, with bond lengths of 2.30(Re-B), 1.88(Re-B),

and 1.88(Re-B) Å, respectively. The values of the shortest Re-B and B-B bond lengths are much smaller than those in $P6_3/mmc$ one. Therefore, the $P\bar{6}m2$ phase may be more stable than the $P6_3/mmc$ one, which is in accordance with the results of calculated formation energies in Table I. Therefore, the $P\bar{6}m2$ phase is the ground-state phase of ReB_3 . The $P\bar{3}m1$ phase contains a puckered hexagonal planar boron layer formed by B-B bonds. In this phase, each rhenium atom is coordinated by three boron atoms. Moreover, these are two types boron atoms in the $P\bar{3}m1$ phase. One is coordinated by one boron atom and one rhenium atom, and the other is coordinated by two boron atoms and one rhenium atom. The positive formation energy of this phase implies that it will be prone to decompose in the course of synthesis.

For IrB_3 , four structures have been predicted. Their symmetries are $Amm2$, $P6_3/mmc$, $P\bar{6}m2$, and $P\bar{3}m1$, respectively. The $Amm2$ phase is the most stable structure because of the negative and lowest formation energy at 0 GPa. Therefore, it is the ground-state phase of IrB_3 . The boron atoms in $Amm2\text{-IrB}_3$ form stable triangle. The shortest Ir-B and B-B bond lengths are 2.14 and 1.71 Å, respectively. The $P6_3/mmc$ phase has the similar structure with $P6_3/mmc\text{-ReB}_3$. Each iridium atom is coordinated by four boron atoms. There are two types boron atoms in $P6_3/mmc\text{-IrB}_3$. One is coordinated by one iridium atom and two boron atoms, with bond lengths of 2.28(Re-B), 1.59(B-B), and 1.87(B-B) Å, respectively. The other is coordinated by two iridium atoms and two boron atoms, with bond lengths of 2.32(Re-B) and 1.87(B-B) Å, respectively. The shortest Ir-B and B-B bond lengths are 2.28 and 1.59 Å, respectively. The negative formation energy and the short B-B bond indicate that it is stable. The $P\bar{6}m2$ phase has a consistent architecture with $P\bar{6}m2\text{-ReB}_3$. Each iridium atom is coordinated by three boron atoms. There are also two types boron atoms in $P\bar{6}m2$ phase. One is coordinated by one iridium atom and two boron atoms, with bond lengths of 2.32(Re-B) and 1.78(B-B) Å, respectively. The other is coordinated by one iridium atom and two boron atoms with bond lengths of 2.28(Re-B), 1.59(B-B), and 1.87(B-B) Å, respectively. The shortest Ir-B and B-B bond lengths are 2.28 and 1.59 Å, respectively. $P\bar{3}m1\text{-IrB}_3$ is similar to $P\bar{3}m1\text{-ReB}_3$ in structure. The shortest B-B bond length is 1.79 Å. The positive formation energy indicates that it is not stable at 0 GPa.

We calculated the formation enthalpies of these predicted compounds under the pressure range from 0 GPa to 100 GPa shown in Fig. 5. We can see that the most stable phase under zero pressure may not be the most stable one under high pressure. All the enthalpy-pressure

curves show that with the increasing of pressure, the stabilities of these structures gradually increase, suggesting that high pressure is helpful to their stabilities. For ReB_3 , the $P\bar{6}m2$ phase and the $P6_3/mmc$ phase are thermodynamically stable at 0 GPa. Especially, the $P\bar{6}m2$ phase is always the most stable phase under the whole studied pressure range. The $P\bar{3}m1$ phase becomes thermodynamically stable phase when the pressure is above 5 GPa. For IrB_3 , the $Amm2$ phase is the most stable phase under the whole studied pressure range. The $P\bar{3}m1$ phase becomes stable when the pressure is above 40 GPa.

To compare the stability of the predicted ReB_3 with ReB_2 and IrB_3 with IrB_2 , we calculated the enthalpy of each predicted structure relative to that of $P6_3/mmc\text{-ReB}_2$ [31] and $Pm\bar{m}n\text{-IrB}_2$ [22], respectively, as shown in Fig. 6. The enthalpies of Re, Ir, B, ReB_2 , and IrB_2 in this figure are our calculation results at the corresponding pressures. From Fig. 6 (a), at low pressure, ReB_2 is more stable than all the structures of ReB_3 , which indicates that these ReB_3 may decompose into ReB_2 and B at low pressure. $P\bar{6}m2\text{-ReB}_3$ becomes more stable than ReB_2 with the pressure increasing to 37 GPa. In Fig. 6 (b), under low pressure, IrB_2 is more stable than all the structures of IrB_3 . However, IrB_3 with the phases of $Amm2$, $P6_3/mmc$, $P\bar{6}m2$, and $P\bar{3}m1$ become more stable than IrB_2 as the pressure increasing to 7 GPa, 28 GPa, 33 GPa, and 73 GPa, respectively. Thus, $P\bar{6}m2\text{-ReB}_3$, and IrB_3 with symmetry of $Amm2$, $P6_3/mmc$, $P\bar{6}m2$, and $P\bar{3}m1$ can be synthesized at high pressure.

B. Dynamical Stability and Elastic Properties

Dynamic stability is very important for a new structure to be existed, because the appearance of soft phonon modes can lead to its distortion. For example, Cheng et al. calculated the phonon dispersion curves of WB_3 with symmetry of $P6_3/mmc$, $R\bar{3}m$, $P\bar{6}m2$, and $P\bar{3}m1$, and found no imaginary phonon frequency appearing in the whole Brillouin zone of them, illustrating that they are dynamically stable.[15] In view of this, we calculated the phonon dispersion curves at 0 GPa to check the dynamical stabilities of the currently predicted structures of ReB_3 and IrB_3 . The phonon dispersion curves of ReB_3 and IrB_3 are shown in Fig. 8 and Fig. 9, respectively. We can see that no imaginary phonon frequency appears in the whole Brillouin zone of these predicted structures. This confirms that all of these predicted compounds are dynamically stable at 0 GPa. Comparing these phonon dispersion curves, for long wave-length limitation, the transverse acoustic wave velocity of $P6_3/mmc\text{-ReB}_3$ is largest. In other words, $P6_3/mmc\text{-ReB}_3$ has the highest shear wave velocity among these compounds. That is to say, $P6_3/mmc\text{-ReB}_3$ may have the strongest ability to against

applied shear deformation. The highest shear modulus of $P6_3/mmc$ - ReB_3 among these structures in Table II confirms this conclusion.

Mechanical stability is one necessary condition for the existence of a crystal. Accurate elastic constants can not only help us to understand the mechanical properties but also provide very useful information to estimate the hardness of a compound. To be mechanically stable, the elastic stiffness constants of a given crystal should satisfy the generalized elastic stability criteria.[32] The calculated elastic constants with the strain-stress method are listed in Table II. Obviously, the elastic constants of all the studied compounds can satisfy with the mechanical stability criteria, indicating that they are all mechanically stable. The positive eigenvalues of the elastic constants matrix for these compounds further prove that they are elastically stable. The elastic constants of these predicted compounds were drawn in Fig. 7. As seen in this figure, C_{44} , C_{55} , and C_{66} for these compounds are close. The values of C_{33} of these predicted compounds are much larger than those of C_{11} and C_{12} , except of $Amm2$ - IrB_3 . C_{11} , C_{22} , and C_{33} of these compounds are larger than 400 GPa, indicating the strong incompressibility along a -axis, b -axis, and c -axis, respectively. Among these compounds, $P\bar{6}m2$ - ReB_3 has extremely large C_{33} which is much larger than that of C_{11} , indicating that the bond strength along the [001] direction is much stronger than that along the [100] direction. C_{44} is an important indicator for the hardness of materials. All the studied structures have large C_{44} values. Notably, $P\bar{6}m2$ - ReB_3 possesses the largest C_{44} value, indicating its relatively strong strength to against shear deformation.

Bulk and shear moduli are important indicators for the hardness of a material. The calculated elastic constants were used to estimate the bulk and shear modulus of ReB_3 and IrB_3 with Voigt-Reuss-Hill (VRH) approximation. Moreover, the bulk modulus (B_0) was also calculated using the third order Birch-Murnaghan equation, and the obtained values are consistent with the bulk modulus (B), implying the reliability of the present theoretical method. As known that, the high bulk modulus of a material illustrates its strong ability to resist volume deformation caused by an applied load. Apparently, all the predicted compounds in Table II have large bulk modulus (above 260 GPa), indicating that they are difficult to be compressed. Compared with the bulk modulus, the shear modulus (G) is a much better parameter to indicate the hardness of a material. From Table II, all structures of ReB_3 possess high shear modulus. Among them, $P6_3/mmc$ - ReB_3 has the largest shear modulus (258 GPa), indicating that it can withstand the largest extent shear strain. In

contrast, the shear moduli of all the structures of IrB_3 are below 200 GPa, indicating the relative low resistance to shape change at a constant volume.

We also list the ratio value of B/G , Young's modulus Y , and Poisson's ratio ν . The ratio value of B/G is a criterion to describe the ductility or brittleness of materials with 1.75 as the critical value.[32] A B/G value higher (or lower) than the criteria is considered to be ductile (or brittle). From Table II, except $Amm2\text{-IrB}_3$, $P6_3/mmc\text{-IrB}_3$, and $P\bar{6}m2\text{-IrB}_3$, the B/G values of other predicted phases are under the critical value, implying their brittle nature. The Young's modulus, Y , indicates the capability of resisting tension and pressure in the range of elastic deformation. A large value of Y manifests a stiff material. From Table II, we can see that $P6_3/mmc\text{-ReB}_3$ will be much stiffer than other studied compounds due to its largest Y (610 GPa).

Poisson's ratio ν is the ratio between transverse and longitudinal strain in the elastic loading direction. Thus, it can be used to describe the degree of directionality for the covalent bond. Materials with small Poisson's ratio are more easily compressed than sheared (small B/G), whereas those with high Poisson's ratio resist compression in favor of shear (large B/G).[33] The small Poisson's ratio implies the strong degree of directionality of covalent bonding in a material. As shown in Table II, all the studied compounds have small Poisson's ratios ν . Especially, $P6_3/mmc\text{-ReB}_3$ (0.18) has a smaller ν than those of ReB_2 (0.21[34] and 0.19[18]) and WB_4 (0.34[35]), indicating its strong degree of directionality of covalent bonding in $P6_3/mmc\text{-ReB}_3$.

As a fundamental parameter, Debye temperature correlates with many physical properties of a solid, such as specific heat, elastic constants, and melting temperature. At low temperature, the calculated Debye temperature from elastic constants is same as that one which is determined from specific heat measurements. In this work, we calculated Debye temperature of the studied compounds and list them in Table II. Debye temperature can represent the characterization and the microhardness of a solid.[36, 37] $P6_3/mmc\text{-ReB}_3$ has the highest Debye temperature of 789 K, which is comparable to that of ReB_2 (755.5 K,[38] 858.3 K[39]). Therefore, $P6_3/mmc\text{-ReB}_3$ may have the largest hardness among these predicted compounds.

The hardness of a material is the intrinsic resistance to deformation when a force is applied, which depends on the loading force and the quality of the sample (i.e., the presence of defects such as vacancies and dislocations).[40, 41] In this work, we adopted the first-

principle model of Chen et al.[41, 42] to figure out the theoretical hardness of the predicted ReB_3 and IrB_3 . The hardness is defined by:

$$H_v(\text{GPa}) = 2(k^2G)^{0.585} - 3, \quad (1)$$

where H_v , k , and G are the Vickers hardness (GPa), Pugh modulus ratio $k = G/B$, [43] and shear modulus (GPa), respectively. Table II lists the calculated hardness of the predicted structures. $P6_3/mmc\text{-ReB}_3$ possesses a large hardness of 37 GPa, which is close to the superhard limit of 40 GPa, indicating that it is a promising superhard material. $P\bar{6}m2\text{-ReB}_3$ also possesses a large hardness of 30 GPa next to $P6_3/mmc\text{-ReB}_3$. We hope it can be the excellent candidate of superhard materials.

C. Electronic Structure and Chemical Bonding

To further understand the electronic structures and chemical bonding of these triborides, we calculated the total and partial density of states at zero pressure, and display them in Fig. 3 and Fig. 10. Clearly, the finite electronic DOS at the Fermi level indicates that all the predicted structures are metallic. It is easy to see that the peaks below -9 eV are mainly attributed to B-s states with a slight contribution from B-p, M(Re and Ir)-p, and M-d states. The states above -9 eV mainly originate from M-d and B-p orbitals with little contributions of M-p and B-s orbitals. The DOSs of M-d and B-p have a similar shape, indicating a strong hybridization between M-5d and B-2p orbitals. This hybridization could herald strong M-B bonding in these compounds, especially in $P\bar{6}m2\text{-ReB}_3$. Another typical feature of DOS is pseudogap, which is the borderline between bonding and antibonding states.[44] For $P\bar{6}m2\text{-ReB}_3$, and $Amm2\text{-IrB}_3$, the presence of pseudogap at the Fermi level suggests that their high stability. The pseudogap also implies the relatively stronger bonding between M and B atoms in these structures. For $P6_3/mmc\text{-IrB}_3$, the pseudogap appears below the Fermi energy, indicating full and partial occupancy of the bonding and antibonding states, respectively.

To gain a deeply understanding of the bonding feature, we calculated the electronic localization function (ELF) of all the structures we predicted, which can characterize electron pairing and localization. ELF is based on the Hartree-Fock pair probability of parallel spin electrons and is widely used to describe and visualize chemical bonding in molecules and solids.[45] ELF values are scaled between 0 and 1, the upper limit $\text{ELF} = 1$ corresponds to the perfect localization characteristic of covalent bonds or lone pairs, while $\text{ELF} = 0.5$ represents

an electron-gas-like pair probability with values of this order indicating regions with bond of a metallic character, and $ELF = 0$ is typical for a vacuum (no electron density) or areas between atomic orbitals. Therefore, the ELF is useful in distinguishing metallic, covalent, and ionic bond, and should not be equated with electron density. The color contour maps of the calculated ELF are shown in Fig. 4. In this figure, high electron localization can be seen in the region between adjacent B atoms, indicating the existence of strong covalent B-B bonding. This strong covalent B-B bonding may result in their large hardness. In $P\bar{6}m2$ - ReB_3 , the largest value of ELF between B atoms is 0.805, indicating a very strong covalent B-B bonding in it. The local maximum values of ELF between Re and B atoms reach 0.75, indicating the covalent bonding feature between Re and B atoms. A similar situation appears in $P6_3/mmc$ - ReB_3 . These strong covalent B-B bonding and Re-B bonding can be the source for their high hardness and stability. However, in these compounds, the local maximum values of ELF between M and B atoms are very close to the B sites, indicating partial covalent and ionic interactions between M and B atoms. Moreover, the values of ELF near the center of the M and B atoms are all close to 0.5, signifying a partially metallic feature in the M-B bond.

IV. CONCLUSION

Using the developed particle swarm optimization algorithm, we predicted the possible crystal structures of ReB_3 and IrB_3 , and investigated their structures, phase stability, dynamical stability, elastic properties, and electronic properties by using first principles calculations based on density functional theory. We predicted two structures of ReB_3 with the symmetry of $P6_3/mmc$ and $P\bar{6}m2$. They are more stable than the experimental one. Their negative formation energies suggest that they can exist at atmospheric pressure. The ground-state phases of ReB_3 and IrB_3 are $P\bar{6}m2$ - ReB_3 and $Amm2$ - IrB_3 , respectively. These compounds are dynamically stable at zero pressure. The calculated elastic constants indicate they are all mechanically stable. The high bulk modulus of these compounds indicate their low compressibility. The high shear moduli of $P\bar{6}m2$ - ReB_3 and $P6_3/mmc$ - ReB_3 suggest their strong ability to against the shape change at a constant volume. The calculated DOSs show that they are all metallic. The results of the calculated electronic localization function show the strong covalent B-B bond in these structures, which makes a large contribution

to their high hardness. The analysis of DOSs and chemical bonding shows that the strong covalent bonds in these compounds make great contributions to their stabilities. We hope these calculations can stimulate extensive experimental work on these predicted triborides.

V. ACKNOWLEDGMENTS

This research was sponsored by the National Natural Science Foundation of China (No. 21071045 and 51371076) and the Program for Innovative Research Team (in Science and Technology) in University of Henan Province (No. 13IRTSTHN017).

-
- [1] S. A. Grünhaldi, *Réaumur's Memoirs on Steel and Iron, A Translation from the Original Printed in 1722. 396 pages, 17 pl*, 1956.
- [2] V. Brazhkin, N. Dubrovinskaia, M. Nicol, N. Novikov, R. Riedel, V. Solozhenko and Y. Zhao, *Nat. Mater.*, 2004, **3**, 576–577.
- [3] R. Wentorf Jr, *J. Chem. Phys.*, 1957, **26**, 956–956.
- [4] D. M. Teter and R. J. Hemley, *Sci.*, 1996, **271**, 53–55.
- [5] H. Y. Chung, M. B. Weinberger, J. B. Levine, A. Kavner, J. M. Yang, S. H. Tolbert and R. B. Kaner, *Sci.*, 2007, **316**, 436–439.
- [6] A. M. Locci, R. Licheri, R. Orrù and G. Cao, *Ceram. Int.*, 2009, **35**, 397–400.
- [7] W. Zhou, H. Wu and T. Yildirim, *Phys. Rev. B*, 2007, **76**, 184113.
- [8] R. W. Cumberland, M. B. Weinberger, J. J. Gilman, S. M. Clark, S. H. Tolbert and R. B. Kaner, *J. Am. Chem. Soc.*, 2005, **127**, 7264–7265.
- [9] X. Zhang, G. E. Hilmas and W. G. Fahrenholtz, *Mater. Lett.*, 2008, **62**, 4251–4253.
- [10] H. Niu, J. Wang, X. Q. Chen, D. Li, Y. Li, P. Lazar, R. Podloucky and A. N. Kolmogorov, *Phys. Rev. B*, 2012, **85**, 144116.
- [11] R. Mohammadi, A. T. Lech, M. Xie, B. E. Weaver, M. T. Yeung, S. H. Tolbert and R. B. Kaner, *Proc. Natl. Acad. Sci. U.S.A.*, 2011, **108**, 10958–10962.
- [12] Q. Li, D. Zhou, W. Zheng, Y. Ma and C. Chen, *Phys. Rev. Lett.*, 2013, **110**, 136403.
- [13] Y. Liang, Y. Gou, X. Yuan, Z. Zhong and W. Zhang, *Chem. Phys. Lett.*, 2013, **580**, 48–52.

- [14] X. Cheng, W. Zhang, X. Q. Chen, H. Niu, P. Liu, K. Du, G. Liu, D. Li, H.-M. Cheng and H. Ye, *Appl. Phys. Lett.*, 2013, **103**, 171903.
- [15] X. Y. Cheng, X. Q. Chen, D. Z. Li and Y. Y. Li, *Acta Crystallogr. Sect. C*, 2014, **70**, 85–103.
- [16] B. Aronsson, E. Stenberg and J. Aselius, *Acta Chem. Scand.*, 1960, **14**, 733–741.
- [17] H. Gou, Z. Wang, J. Zhang, S. Yan and F. Gao, *Inorg. Chem.*, 2009, **48**, 581–587.
- [18] E. Zhao, J. Wang, J. Meng and Z. Wu, *J. Comput. Chem.*, 2010, **31**, 1904–1910.
- [19] J. Rau and A. Latini, *Chem. Mater.*, 2009, **21**, 1407–1409.
- [20] A. Latini, J. V. Rau, R. Teghil, A. Generosi and V. R. Albertini, *ACS Appl. Mater. Interfaces*, 2010, **2**, 581–587.
- [21] W. J. Zhao and Y. X. Wang, *J. Solid State Chem.*, 2009, **182**, 2880–2886.
- [22] D. Y. Wang, B. Wang and Y. X. Wang, *J. Phys. Chem. C*, 2012, **116**, 21961–21966.
- [23] Y. Wang, J. Lv, L. Zhu and Y. Ma, *Phys. Rev. B*, 2010, **82**, 094116.
- [24] Y. Wang, J. Lv, L. Zhu and Y. Ma, *Comput. Phys. Commun.*, 2012, **183**, 2063–2070.
- [25] G. Kresse and D. Joubert, *Phys. Rev. B*, 1999, **59**, 1758.
- [26] G. Kresse and J. Hafner, *Phys. Rev. B*, 1993, **47**, 558.
- [27] R. Hill, *Proc. Phys. Soc. London, Sect. A*, 1952, **65**, 349.
- [28] Z. W. Ji, C. H. Hu, D. H. Wang, Y. Zhong, J. Yang, W. Q. Zhang and H. Y. Zhou, *Acta Mater.*, 2012, **60**, 4208–4217.
- [29] Y. Liang, X. Yuan and W. Zhang, *Phys. Rev. B*, 2011, **83**, 220102.
- [30] R. Zhang, D. Legut, Z. Lin, Y. Zhao, H. Mao and S. Veprek, *Phys. Rev. Lett.*, 2012, **108**, 255502.
- [31] V. Telegus, Y. B. Kuz'ma and T. K. Stefanishina, *Powder Metallurgy and Metal Ceramics*, 1969, **8**, 133–136.
- [32] Z. Wu, E. Zhao, H. Xiang, X. Hao, X. Liu and J. Meng, *Phys. Rev. B*, 2007, **76**, 054115.
- [33] T. Rouxel, H. Ji, J. Guin, F. Augereau and B. Rufflé, *J. Appl. Phys.*, 2010, **107**, 094903.
- [34] Y. X. Wang, *Appl. Phys. Lett.*, 2007, **91**, 101904–101904.
- [35] E. Zhao, J. Meng, Y. Ma and Z. Wu, *Phys. Chem. Chem. Phys.*, 2010, **12**, 13158–13165.
- [36] D. B. Sirdeshmukh, L. Sirdeshmukh and K. Subhadra, *Micro-and macro-properties of solids: thermal, mechanical and dielectric properties*, Springer, 2006, vol. 80.
- [37] S. Abrahams and F. Hsu, *J. Chem. Phys.*, 1975, **63**, 1162–1165.
- [38] S. Aydin and M. Simsek, *Phys. Rev. B*, 2009, **80**, 134107.

- [39] X. Hao, Y. Xu, Z. Wu, D. Zhou, X. Liu, X. Cao and J. Meng, *Phys. Rev. B*, 2006, **74**, 224112.
- [40] J. Tse, *J. Superhard Mater.*, 2010, **32**, 177–191.
- [41] X. Q. Chen, H. Niu, C. Franchini, D. Li and Y. Li, *Phys. Rev. B*, 2011, **84**, 121405.
- [42] X. Q. Chen, H. Niu, D. Li and Y. Li, *Intermetallics*, 2011, **19**, 1275–1281.
- [43] S. Pugh, *Philos. Mag.*, 1954, **45**, 823–843.
- [44] P. Vajeeston, P. Ravindran, C. Ravi and R. Asokamani, *Phys. Rev. B*, 2001, **63**, 045115.
- [45] A. D. Becke and K. E. Edgecombe, *J. Chem. Phys.*, 1990, **92**, 5397–5403.

TABLE I. Calculated formation energy per unit (ΔH), optimized equilibrium lattice parameters a and c (\AA), density (ρ in g/cm^3), and atom volume (V in $\text{\AA}^3/\text{atom}$) of ReB_3 and IrB_3 .

	Space group	ΔH	a	c	ρ	V
ReB_3	$P-6m2$ (187)	-0.287	2.9235	4.5953	10.736	8.50
ReB_3	$P6_3/mmc$ (194)	-0.012	2.9044	9.3134	10.925	8.36
	$P6_3/mmc$ (194) ^a	0.7300	3.0960	7.5730		
	$P6_3/mmc$ (194) ^b		2.9000	7.4750		
ReB_3	$P-3m1$ (164)	0.0222	2.8743	4.6734	10.929	8.35
IrB_3	$Amm2$ (38)	-0.671	5.3106	2.8456	10.739	8.73
IrB_3	$P6_3/mmc$ (194)	-0.018	2.9324	9.2820	10.855	8.64
IrB_3	$P-6m2$ (187)	-0.004	2.9282	4.6450	10.878	8.62
IrB_3	$P-3m1$ (164)	0.1585	2.8727	4.6665	11.249	8.34

^a Ref.[18], VASP

^b Ref.[16], experiment

TABLE II. Calculated elastic constants (in GPa), bulk modulus (B , B_0 in GPa), shear modulus (G in GPa), Young's modulus (Y in GPa), Poisson's ratio ν , Debye temperature (Θ_D in K), and hardness (H_v in GPa) of ReB_3 and IrB_3 .

	C_{11}	C_{12}	C_{13}	C_{33}	C_{44}	C_{66}	$B(B_0)$	G	B/G	Y	ν	Θ_D	H_v
$\text{ReB}_3(P-6m2)$	567	130	175	905	229	218	333(320)	239	1.39	579	0.21	764	30
$\text{ReB}_3(P6_3/mmc)$	665	128	123	809	217	269	321(320)	258	1.24	610	0.18	789	37
$\text{ReB}_3(P-3m1)$	613	177	122	795	194	218	318(317)	228	1.39	552	0.21	744	29
$\text{IrB}_3(Amm2)$	475	277	120	486	184	164	285(286)	157	1.82	398	0.27	617	16
$\text{IrB}_3(P6_3/mmc)$	398	172	223	643	164	113	297(283)	143	2.08	370	0.29	590	13
$\text{IrB}_3(P-6m2)$	414	182	206	666	125	116	298(286)	133	2.24	347	0.31	570	11
$\text{IrB}_3(P-3m1)$	556	176	147	666	131	190	302(302)	178	1.70	446	0.25	651	19
diamond	1047	128			560		434	564	0.77	1181	0.05		

FIGURE CAPTIONS

- : Fig. 1. Crystal structures of ReB_3 . The blue and gray spheres represent Re and B atoms, respectively. (a) $\text{ReB}_3(P\bar{6}m2)$: No. 187, the Re atom is at 1b (1, 0, 0.5000), and the B atom has two sites: 2h (0.3333, 0.6667, 0.1805), 1a (1, 0, 0); (b) $\text{ReB}_3(P6_3/mmc)$: No. 194, the Re atom is at 2a (0, 0, 0), and the B atom has two sites: 4f (0.3333, 0.6667, 0.6626), 2b (0, 1, 1/2); (c) $\text{ReB}_3(P\bar{3}m1)$: No. 164, the Re atom is at 1a (0, 0, 0), and the B atom has two sites: 2d (0.6667, 0.3333, 0.3320), 1b (0, 0, 0.5000); (d) experimental $\text{ReB}_3(P6_3/mmc)$: No. 194.
- : Fig. 2. Crystal structures of IrB_3 . The sallow and gray spheres represent Ir and B atoms, respectively. (a) $\text{IrB}_3(Amm2)$: No. 38, the Ir atom is at: 4e (0.5000, 0.1772, 0.6254), and the B atom has three sites 4e (0.5000, 0.0933, 0.2501); (b) $\text{IrB}_3(P6_3/mmc)$: No. 194, the Ir atom is at: 2a (0, 0, 0), and the B atom has two sites 2b (0, 1, 0.7500); (c) $\text{IrB}_3(P\bar{6}m2)$: No. 187, the Ir atom is at: 1d (0.3333, 0.6667, 0.5000) and the B atom has two sites: 1c (0.3333, 0.6667, 0), 2i (0.6667, 0.3333, 0.8288); (d) $\text{IrB}_3(P\bar{3}m1)$: No. 164, the Ir atom is at: 1b (0, 0, 0.5000) and the B atom has two sites 2d (0.3333, 0.6667, 0.1443), 1a (0, 0, 0).
- : Fig. 3. Calculated total and partial DOS of ReB_3 . The Fermi level is at zero.
- : Fig. 4. Contours of the electronic localization function (ELF) of (a) experimental $\text{ReB}_3(P6_3/mmc)$, (b) $\text{ReB}_3(P\bar{6}m2)$, (c) $\text{ReB}_3(P6_3/mmc)$, (d) $\text{ReB}_3(P-3m1)$, (e) $\text{IrB}_3(Amm2)$, (f) $\text{IrB}_3(P-6m2)$, (g) $\text{IrB}_3(P6_3/mmc)$, (h) $\text{IrB}_3(P-3m1)$.
- : Fig. 5. Relative formation enthalpy-pressure of (a) ReB_3 and (b) IrB_3
- : Fig. 6. Calculated enthalpy under pressure of ReB_3 and IrB_3 relative to ReB_2 and IrB_2 , respectively: (a) ReB_3 relative to the ReB_2 (b) IrB_3 relative to the IrB_2
- : Fig. 7. Calculated elastic constants of ReB_3 and IrB_3 .
- : Fig. 8. Phonon dispersion curves of ReB_3 at 0 GPa.
- : Fig. 9. Phonon dispersion curves of IrB_3 at 0 GPa.
- : Fig. 10. Calculated total and partial DOS of IrB_3 . The Fermi level is at zero.

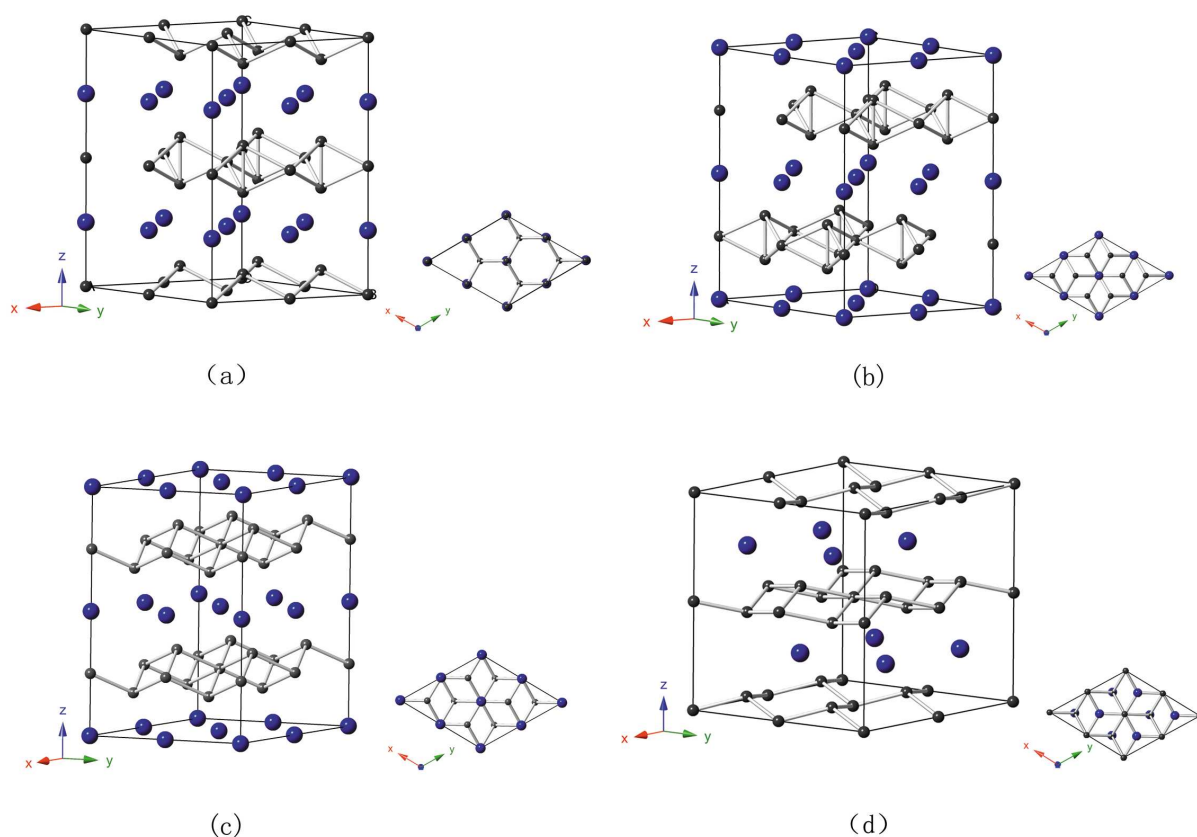


FIG. 1. Crystal structures of ReB_3 . The blue and gray spheres represent Re and B atoms, respectively. (a) $\text{ReB}_3(P\bar{6}m2)$: No. 187, the Re atom is at 1b (1, 0, 0.5000), and the B atom has two sites: 2h (0.3333, 0.6667, 0.1805), 1a (1, 0, 0); (b) $\text{ReB}_3(P6_3/mmc)$: No. 194, the Re atom is at 2a (0, 0, 0), and the B atom has two sites: 4f (0.3333, 0.6667, 0.6626), 2b (0, 1, 1/2); (c) $\text{ReB}_3(P\bar{3}m1)$: No. 164, the Re atom is at 1a (0, 0, 0), and the B atom has two sites: 2d (0.6667, 0.3333, 0.3320), 1b (0, 0, 0.5000); (d) experimental $\text{ReB}_3(P6_3/mmc)$: No. 194.

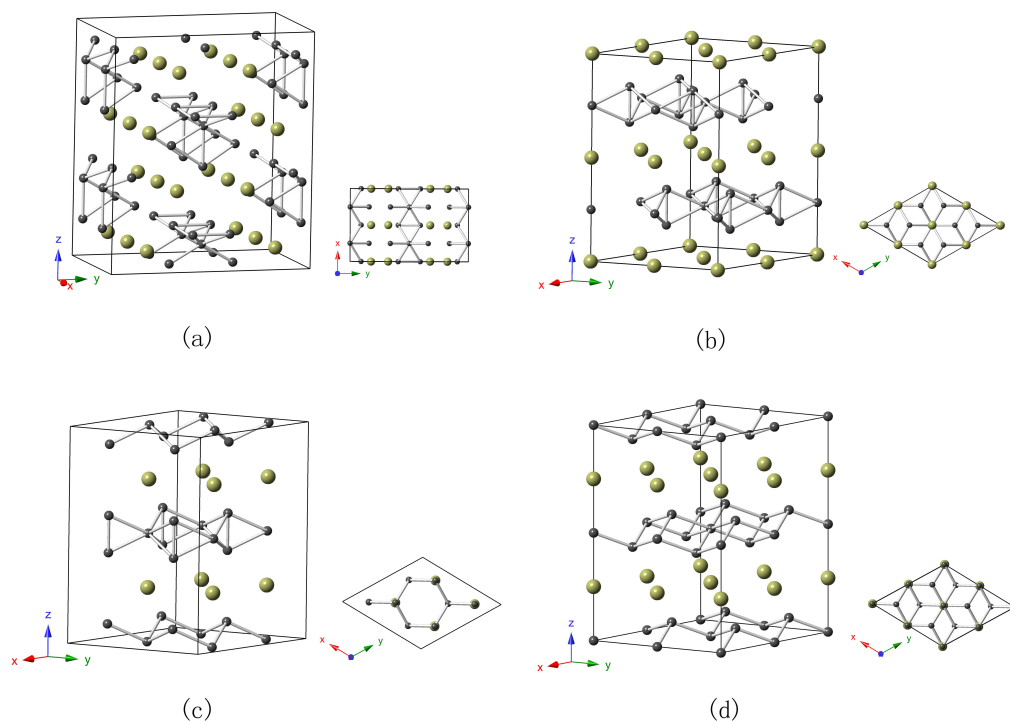


FIG. 2. Crystal structures of IrB_3 . The sallow and gray spheres represent Ir and B atoms, respectively. (a) $\text{IrB}_3(\text{Amm}2)$: No. 38, the Ir atom is at: 4e (0.5000, 0.1772, 0.6254), and the B atom has three sites 4e (0.5000, 0.0933, 0.2501); (b) $\text{IrB}_3(\text{P}6_3/\text{mmc})$: No. 194, the Ir atom is at: 2a (0, 0, 0), and the B atom has two sites 2b (0, 1, 0.7500); (c) $\text{IrB}_3(\text{P}\bar{6}m2)$: No. 187, the Ir atom is at: 1d (0.3333, 0.6667, 0.5000) and the B atom has two sites: 1c (0.3333, 0.6667, 0), 2i (0.6667, 0.3333, 0.8288); (d) $\text{IrB}_3(\text{P}\bar{3}m1)$: No. 164, the Ir atom is at: 1b (0, 0, 0.5000) and the B atom has two sites 2d (0.3333, 0.6667, 0.1443), 1a (0, 0, 0).

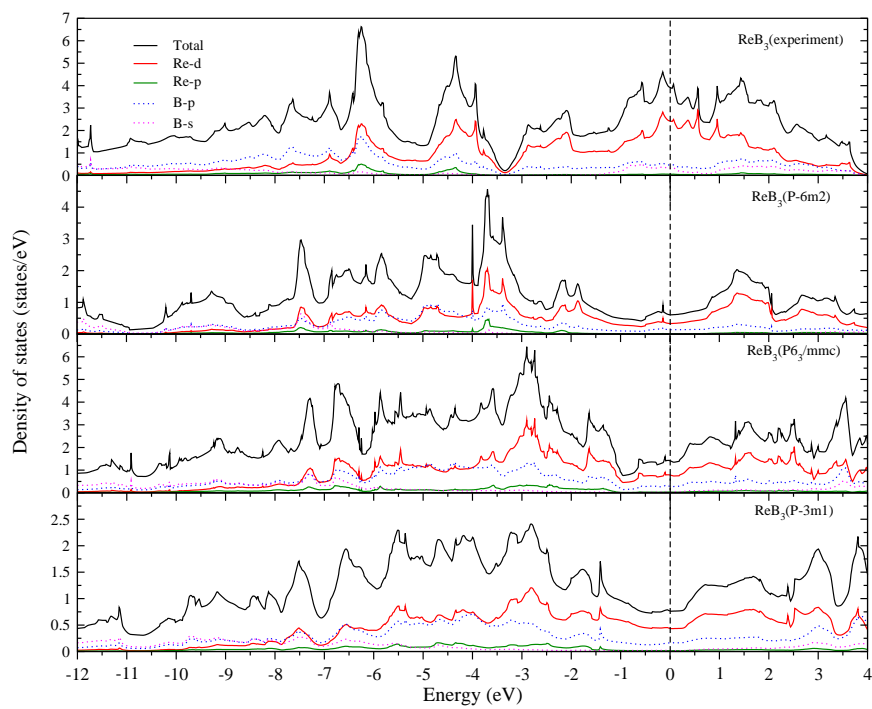


FIG. 3. Calculated total and partial DOS of ReB_3 . The Fermi level is at zero.

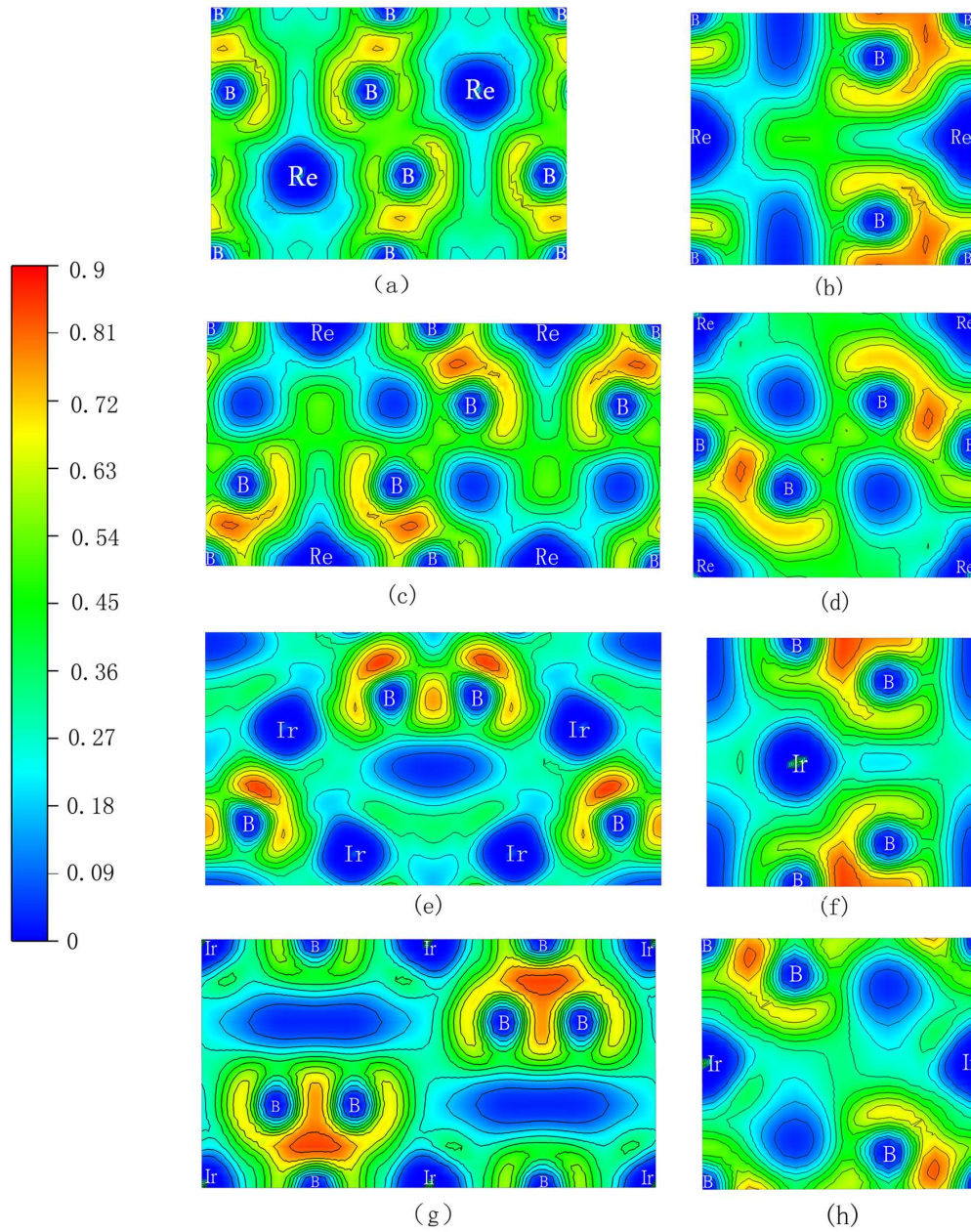


FIG. 4. Contours of the electronic localization function (ELF) of (a) experimental $\text{ReB}_3(P6_3/mmc)$, (b) $\text{ReB}_3(P\bar{6}m2)$, (c) $\text{ReB}_3(P6_3/mmc)$, (d) $\text{ReB}_3(P-3m1)$, (e) $\text{IrB}_3(Amm2)$, (f) $\text{IrB}_3(P-6m2)$, (g) $\text{IrB}_3(P6_3/mmc)$, (h) $\text{IrB}_3(P-3m1)$.

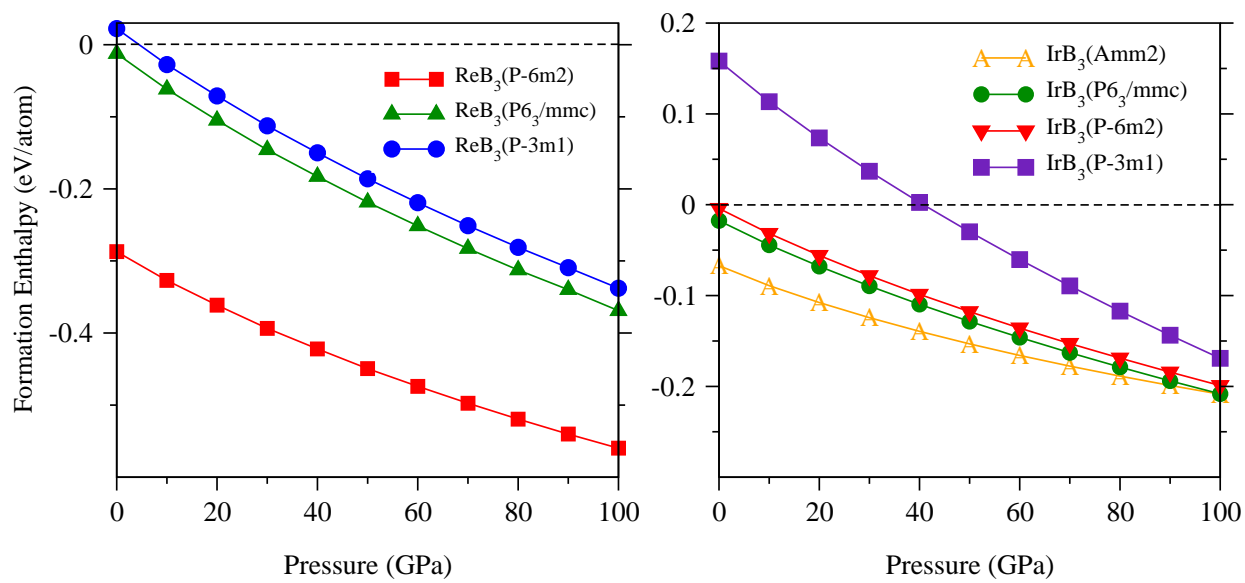


FIG. 5. Relative formation enthalpy-pressure of (a) ReB₃ and (d) IrB₃.

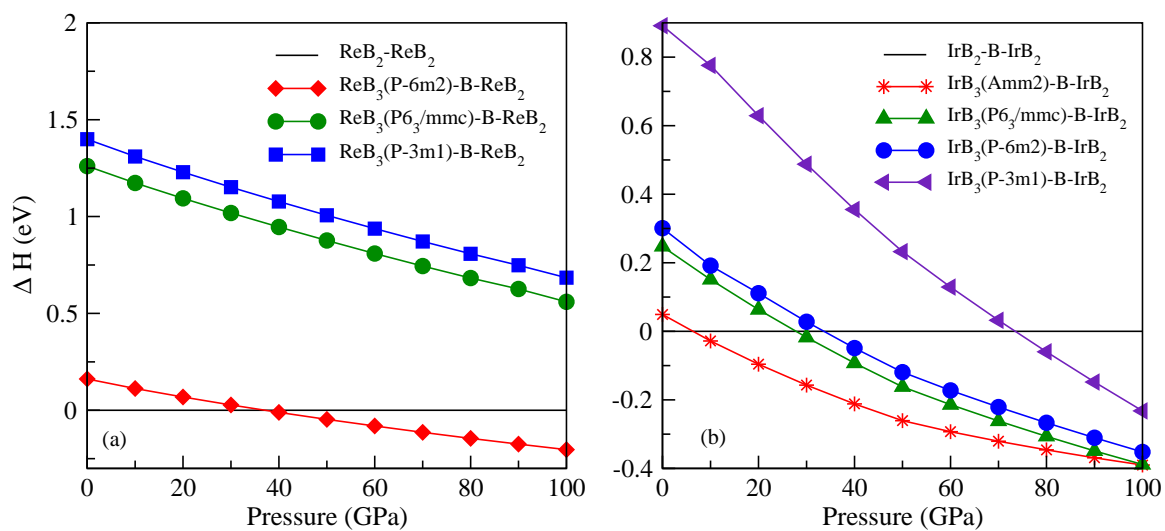
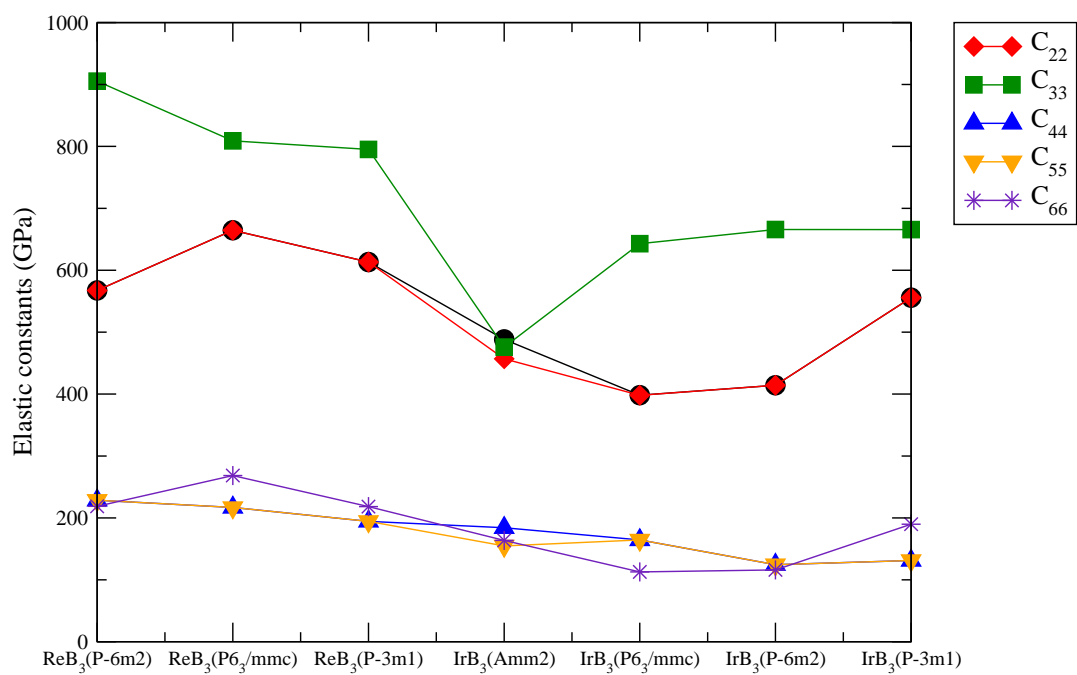
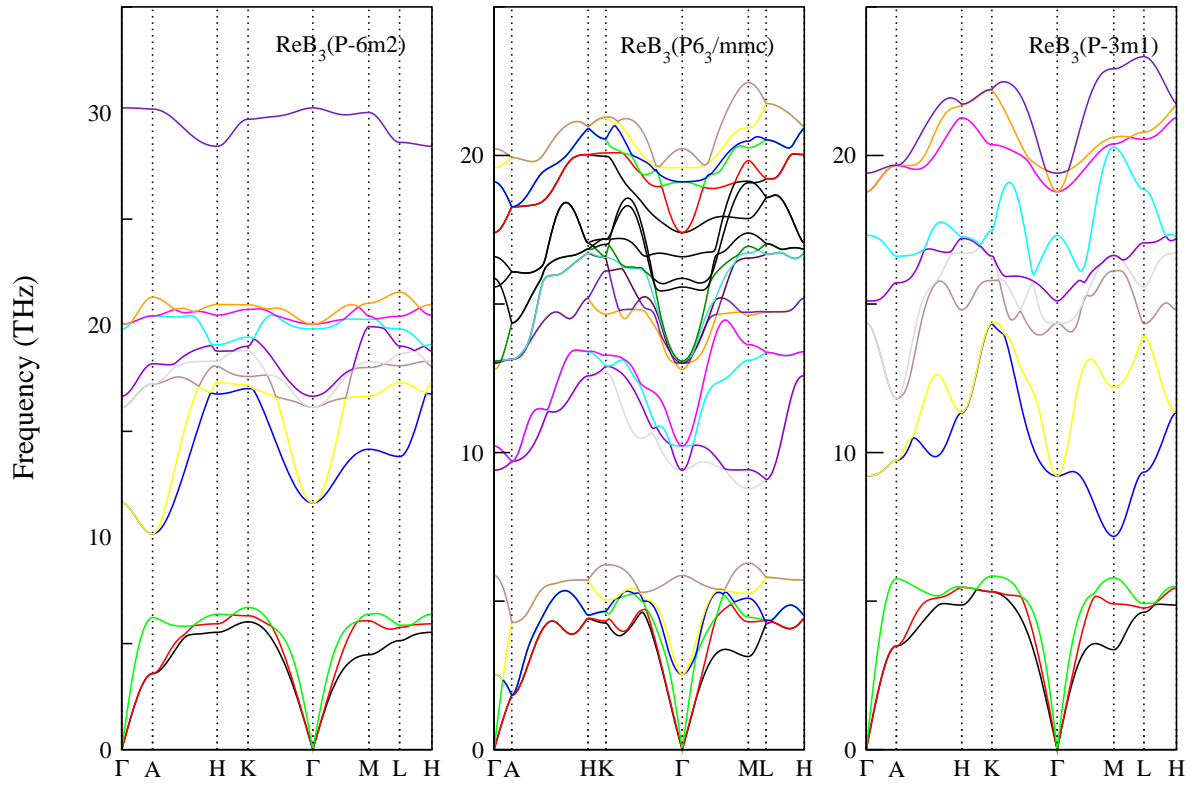


FIG. 6. Calculated enthalpy under pressure of ReB₃ and IrB₃ relative to ReB₂ and IrB₂, respectively: (a) ReB₃ relative to the ReB₂ (b) IrB₃ relative to the IrB₂.

FIG. 7. Calculated elastic constants of ReB₃ and IrB₃.

FIG. 8. Phonon dispersion curves of ReB_3 at 0 GPa.

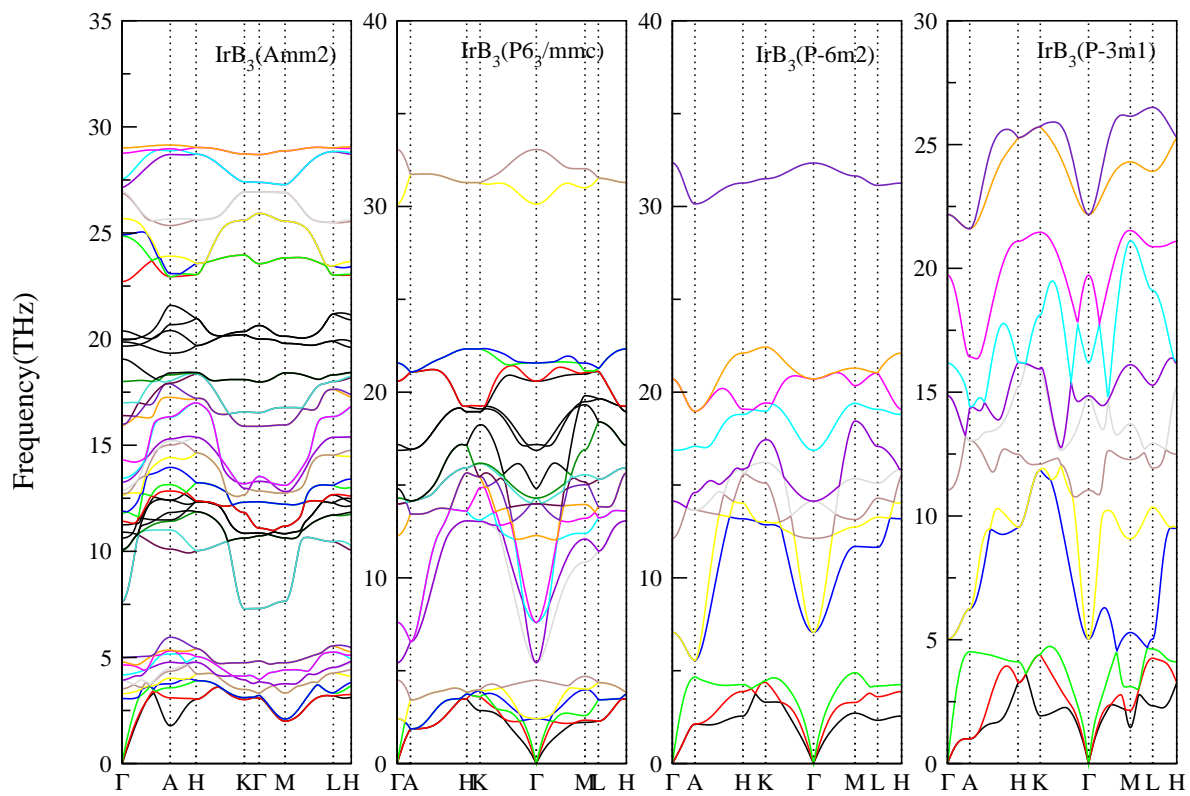


FIG. 9. Phonon dispersion curves of IrB₃ at 0 GPa.

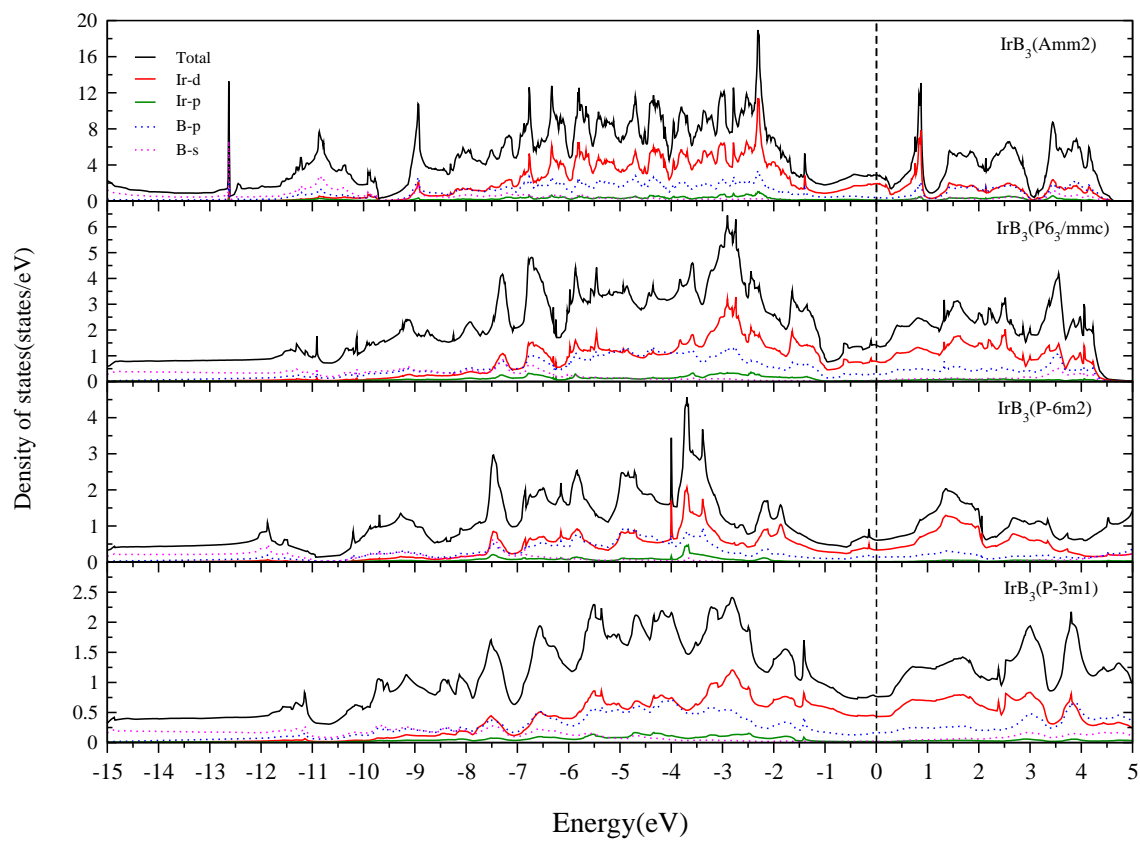


FIG. 10. Calculated total and partial DOS of IrB₃. The Fermi level is at zero.